Metals and Materials International
https://doi.org/10.1007/s12540-024-01786-7

Effect of Different Types of Glass Powders on the Corrosion and Wear Resistance of Peo Coatings Produced on 6061 Aluminum Alloy

Luca Pezzato[1] · Lorena Kostelac[1] · Lavinia Tonelli[2] · Hamada Elsayed[1] · Daniel Kajánek[3] · Enrico Bernardo[1] · Carla Martini[2] · Manuele Dabalà[1] · Katya Brunelli[1]

Received: 18 June 2024 / Accepted: 1 August 2024

Abstract
6061 Aluminium alloy was treated with plasma electrolytic oxidation (PEO) in an alkaline silicate-base electrolyte. Recycled glass particles from consumer goods waste were added to the electrolyte in order to investigate the impact of these particles on corrosion and wear resistance of the alloy. A comparison of glass particles from different sources (liquid crystal display (LCD) glass, borosilicate (BS) glass, and soda-lime (SL) glass) has been made. Also, the effect of different current modes, direct (D) and pulsed (P), on glass incorporation and the coatings morphology was studied. The microstructure and thickness of the produced coatings were studied through SEM–EDS analysis and XRD. The wear resistance was evaluated by dry sliding tests vs AISI 52100 bearing steel (block-on-ring contact geometry). The corrosion behavior was analyzed by potentiodynamic polarization (PDP) and electrochemical impedance spectroscopy (EIS), and localized electrochemical characteristics were determined by scanning electrochemical microscopy (SECM). The results evidenced that the addition of glass improved the corrosion resistance of the samples due to the sealing effect on the typical pores of the PEO layer. In detail samples filled with glass particles show from EIS tests polarization resistances up to one order of magnitude higher than the untreated sample in the case of direct current mode and up to two order of magnitude higher in the case of pulsed current mode. The effect on wear resistance is instead strictly related to the type of glass as, if compared to the base PEO layer, it is improved only by selected additives with the more promising results obtained with the LCD glass in direct current mode that produce a decrease of the wear depth of around one order of magnitude in comparison with the sample PEO treated without glass addition. Globally the more promising type of glass particles, both in term of improvement of the wear and of the corrosion properties, seem to be the LCD glass particles. This fact was related to the particular chemical composition of this type of glass and in particular with the alkali-free composition of the glass.

Keywords Plasma electrokytic oxidation · Aluminun alloys · Corrosion · Wear · Coating

1 Introduction

From space and aerospace to automotive, military equipment and construction metal, aluminium and its alloys are increasingly used in various fields [1–4]. This fact can be related with the numerous properties that it can offer such as high specific strength, exceptional toughness, low density, good electrical and thermal conductivity [1, 3, 5]. In atmospheric exposure, aluminium and aluminium-based alloys are protected by an aluminium oxide film, the thickness of which is 0.005–0.2 µm. This film increases the chemical resistance of materials but cannot guarantee their protection against all types of corrosion. Moreover, when aluminium materials are used in a humid or maritime climate, the surface oxide layer is destroyed and forms a white layer due to corrosion [2]. The most effective way to reduce corrosion is to prepare protective coatings [1, 6].

Plasma electrolytic oxidation (PEO) or micro-arc oxidation (MAO) [7, 8] micro-plasma oxidation, and also anodic spark deposition [9] is a variation of the conventional anodizing method that in situ [10] develops ceramic-like thick

✉ Luca Pezzato
luca.pezzato@unipd.it; lucapezzato@virgilio.it

[1] Department of Industrial Engineering, University of Padova, Via Marzolo 9, 31531 Padua, Italy

[2] Department of Industrial Engineering, University of Bologna, Viale del Risorgimento 4, 40136 Bologna, Italy

[3] Research Centre, University of Žilina, Univerzitná 8215/1, 010 26 Žilina, Slovak Republic

Published online: 24 August 2024

(typically 10 to 100 μm) coatings on valve metals as well as their alloys [5, 11–16]. PEO coatings on aluminium alloys can improve corrosion resistance, wear resistance [4, 14, 17], mechanical hardness [18] thermal stability, electrical properties [9] or induce particular functional properties such as antifouling or fungicidal properties [19].

PEO is a complex process that involves chemical and electrochemical reactions, along with plasma and thermal effects [20]. If the applied potential exceeds the dielectric potential of the oxide coating, numerous micro-discharges with a short lifetime (in milliseconds) are generated at the metal/electrolyte interface during the process. These are the sites on the surface of the metal substrate where the initial formation of the oxide coating takes place [21, 22]. In the case of an aluminium substrate, alumina phases such as α and γ Al_2O_3 typically occur. Micro-discharges result in extremely high localized temperatures and the generation of gases, which contribute to the porous structure of the PEO coating [23–25]. PEO coatings with varying structures, morphological properties, and chemical compositions can be produced by adjusting numerous process parameters, including the applied potential, current density and mode, duty cycle, frequency, PEO treatment duration, and different electrolyte compositions [26]. Among these parameters, the choice of electrolyte plays a crucial role in determining the chemical composition of the coatings, as it leads to the incorporation of electrolyte components into the generated PEO layers. The primary electrolytes used to treat the aluminium matrix are silicate- and phosphate-based alkaline solutions [27, 28]. There is a significant difference in plasma discharge temperatures when using different electrolytes. Silicate-based electrolytes result in much higher temperatures, leading to the formation of crystalline aluminium oxides and mullite. In contrast, phosphate-based electrolytes produce a more amorphous structure with poorer corrosion and wear resistance. Additionally, silicate-based electrolytes offer the advantage of creating more uniform PEO coatings with consistent morphology [27]. It should be emphasized that the advantage of these electrolytes is their environmentally friendly nature [29], unlike the acidic solutions used during anodization [30, 31]. This advantage makes PEO processes particularly attractive today [32]. Although PEO coatings generally enhance corrosion resistance, their porous structure can increase permeability, thereby compromising corrosion resistance. This issue can be mitigated through pore sealing by incorporating various inorganic or organic components into the coatings, and in particular adding as suspension specific particles to the electrolyte [33, 34].

If particles are incorporated without reaction, it is considered inert incorporation. During inert incorporation the size and shape of the particles do not change during the process, and the prsence of the is clearly visible in the layer. The second possibility is reactive or partly reactive incorporation. When reactive or partially reactive incorporation occurs, the high energy discharges of the PEO preocess can melt the particles that after can react with other components from the electrolyte and matrix. The nature of the substrate and of the particles, their melting point and their zeta potetntial, toghether with the composition of the electrolyte and the energy of the discharges, are the main facrors that infleince the process. [15]. The sealing treatment mainly includes organic sealing and inorganic sealing. Compared to organic sealings, inorganic sealings have better mechanical strength, high temperature, and wear resistance [6].

A viable approach to fill the pores within the PEO coating might involve utilizing waste glass powders [3, 4, 8, 9, 17, 28]. This method not only assists in sealing the pores of the PEO coating, thereby enhancing corrosion resistance, but it could also contribute to improving tribological characteristics. Moreover, employing discarded glass material in this manner presents an opportunity to reuse it into new products ("open-loop recycling") [35]. This entails reusing it in items distinct from their initial purpose, also termed "downcycling," to create value-added products [36]. It can benefit both environmental sustainability and energy conservation.

Our previous research, Pezzato et al. [19], investigated the incorporation of borosilicate glass particles and SiC particles on magnesium alloy. We examined the effect on the corrosion and tribological behavior of PEO coatings. The results showed that both SiC and borosilicate glass particles were successful and fully incorporated into PEO coatings. SiC enter trough inert incorporation whereas borosilicate glass particles where partially melted and risolidified forming an amorphus phase. This behavior was related to the different melting points of the compounds. The effect of the particles on the corrosion properties depends on the particle's nature. The addition of SiC particles decreased the corrosion properties due to the conductive nature of SiC. In contrast, the presence of the borosilicate glass particles increased the corrosion properties thank to the sealing of the pores. Considering the wear properties, the best perfomances were obtained by adding glass particles for 3 min treatment time. In this way, wear resistance was increased without the detrimental effects of SiC on the friction coefficient.

Currently, there are not many studies reporting on the inclusion of glass particles in PEO coatings. Glass particles were added to PEO coatings in two articles dealing with magnesium alloys, the one mentioned earlier by our research group and another one by Asgari et al. [9]. According to Asgari, melting glass particles during coating growth enhances corrosion resistance, but no study has examined the effect of glass particles on tribological behavior.

On the other hand, many studies in the literature have investigated the addition of various other particles to the PEO coatings on aluminium alloys, such as α-Al_2O_3, MgO, and TiO_2. Although these particles do not share the same

chemical composition as glass particles, which consist of more than 50% SiO_2, the mechanism of incorporation is mostly similar. O'Hara et al. [37] demonstrated that with the addition of α-Al_2O_3 and MgO particles to the PEO coating, partial melting of the particles occurs. Some particles were incorporated into the pores of the PEO coating without alteration, while others underwent chemical reactions and formed new phases. They also reported that particle incorporation was only possible when the particles were smaller than 10 µm, i.e., smaller than the pore size. Hakimizad et al. [38] obtained a completely inert incorporation of TiO_2 nanoparticles into a PEO coating on a 7075 aluminium alloy. The TiO_2 nanoparticles reduced the coating thickness, increased micro-cracks, and widened the micro-pores of the PEO coating. Similar results were documented by Arrabal et al. [39] who found that addition of α-Al_2O_3 particles to the electrolyte do not significantly affect the size and roughness of the coatings but do influence their morphology. They observed that PEO coatings are decorated with fine α-Al_2O_3 particles that appear to remain intact. They suggested that incorporation may have occurred through direct deposition from the electrolyte following a solution boiling or via electrophoresis, due to the electric field in the electrolyte.

The present research intends to uncover the possibilities associated with utilizing discarded liquid crystal display (LCD) glass, borosilicate (BS) glass, and soda-lime (SL) glass in the PEO treatment process on aluminum alloy 6061. The distinction among these three glass types lies in their varying concentrations of alkaline elements, where SL glass possesses the highest concentration of alkaline elements, whereas LCD glass does not contain any alkaline element (see Table 2). In silica-based glass, the bonding forces responsible for the glass network formation involve crystalline SiO_2. This compound exhibits a tetrahedral structure featuring four O atoms positioned at the corners of a tetrahedron, with a Si atom situated at the structure's center [40]. The introduction of alkali oxides, such as Na_2O, K_2O, and Li_2O, in the glass network is responsible for breaking some of the Si–O–Si bonds and incorporating alkaline cations into the glass structure [40]. The varying concentrations of alkaline elements contribute to the distinct corrosion behaviors observed in glass toghther with different thermal and mechanical properties [40]. In detail an increase in the alkali content produce a decrease in the corrosion properties and a decrease in the mechanical properties. Morehover a decrease in the alkali content produce the formation of a "shorter" glass, charcterized by lower difference between transition temperature and softening temeperature [41]. Therefore, the objective is to investigate how these will influence the corrosion and tribological behavior of PEO coatings containing different types of glass fillers, characterized by different properties due to the different alkaline elements content.

The effect of different current modes, direct and pulsed, on the incorporation of the glass and the morphology of the coatings, was also studied. The microstructure and thickness of the produced coatings were investigated through SEM–EDS analysis and XRD. The wear resistance was evaluated by dry sliding tests vs AISI 52100 bearing steel (block-on-ring contact geometry). The corrosion behavior was analyzed by potentiodynamic polarization (PDP), electrochemical impedance spectroscopy (EIS), and localized electrochemical impedance (LEIS) tests. Novelty of the present work result mainly in the study of the influence of the different types of glasses, and in particular of glasses with different chemical composition, on the wear and corrosion properties of PEO coatings, that was never reported in literature.

2 Experimental Procedure

2.1 PEO Process

Prior to the PEO treatment, samples 4 × 1 cm were cut from 6061 AA plate (nominal composition 1% Mg; 0.0.6% Si; 0.25% Cu; 0.1% Mn; 0.1% Fe; 0,15% Cr; Al bal.)and then polished using conventional metallographic procedures that included a grinding step with abrasive papers (580, 800, 1200, and 4000 grit) and a finishing step with cloths and diamond suspensions (6 µm and 1 µm). Following the polishing, samples were ultrasonically degreased in ethanol for 5 min. An electrolyte bath, carbon-steel mesh as well as cooling and stirring systems were included in the PEO equipment. During the PEO process, a continuous stirring of the electrolyte was applied to prevent concentration and temperature gradients. Aluminium substrate was used as anode, while a carbon-steel mesh was used as cathode. TDK-Lambda 400 V/8 A DC power supply was used for coating production, working in direct (D) and pulsed (P) current modes under a constant current density of 0.65 A/cm^2, 200 Hz frequency and 50% duty cycle for 3 min. In order to perform the PEO process, a base electrolyte (B) and three types of glass were used LCD, BS and SL glass, as indicated in Table 1. High-purity reactants; sodium metasilicate (Na_2SiO_3), and sodium hydroxide (NaOH) were used as base electrolyte. The chemical composition of glass additives is shown in Table 2. The LCD (alkali-free glass), utilized in liquid crystal and OLED displays, came in sizeable sheets from NEG (Nippon Electric Glass Co., Ltd., Ōtsu, Japan). BS originated from a glass cullet (Kimble/Kontes, Vineland, NJ) and was primarily designed for pharmaceutical use. SL was derived from crushed glass containers, furnished in fine powder form by SASIL SpA (Biella, Italy). Notably, all these glasses were sourced from recycled glass materials. Before use, all the employed glasses were reduced into fine

Table 1 Current mode of PEO process and composition of PEO electrolyte.for all the produced samples

Sample	Current mode	Na_2SiO_3 g L^{-1}	NaOH g L^{-1}	LCD glass g L^{-1}	SL glass g L^{-1}	BS glass g L^{-1}
B-D	Direct	25	2.5	–	–	–
B-P	Pulsed	25	2.5	–	–	–
LCD-D	Direct	25	2.5	40	–	–
LCD-P	Pulsed	25	2.5	40	–	–
BS-D	Direct	25	2.5	–	–	40
BS-P	Pulsed	25	2.5	–	–	40
SL-D	Direct	25	2.5	–	40	–
SL-P	Pulsed	25	2.5	–	40	–

powder by dry ball milling (Mixer Mill MM 301, Retsch GmbH) in order to obtain glass particles with coparable size distribution for all the analyzed glasses. In detail the dimension of the obtained glass particles after the ball milling was of micrometric size, varying between 1 and 10 µm. The choiche of the dimensions of the particles was perfoemd in order to assure incorporation into the coating. Further charcterization and studies on all three types of glass can be found in other publications [35, 36, 42].

2.2 Microstructure, Phase Composition and Mechanical Characterisation

A Cambridge Stereoscan 440 scanning electron microscope (SEM), equipped with a Philips PV9800 energy dispersive X-ray spectrometer (EDS) was utilized to analyze the surface and cross-section of samples. When analyzing the cross-section, samples were cut, mounted in epoxy resin, and carefully ground and polished following standard metallographic preparation. The composition analysis was performed on the surface of the samples using EDS. Samples were sputtered with a gold film prior to the SEM analysis. All image analysis was performed using the ImageJ software package [43].

Phase analysis of coatings was studied by a Bruker® X-ray diffractometer (D8 Advance, Karlsruhe, Germany), operating at 40 kV and 40 mA (2θ range between 20° and 90° with a step size of 0.05 and counting time 5 s). All the phases in the coatings were identified using High Score Plus software.

A stylus profilometer (Hommelwerke T2000, 5 µm tip radius) was used to evaluate surface roughness in terms of Ra and Rq, according to ISO 4287 standard (measuring length Lt = 4 mm and sampling length Lc = 0.8 mm). Scratch tests (Revetest, CSM Instruments) were carried out to characterize the practical adhesion of PEO layers. Progressive scratch tests (10 mm length) were performed with a Rockwell diamond indenter (200 µm tip radius) by applying a load from 1 to 30 N and a 10 mm min^{-1} linear speed.

Vickers microhardness tests were conducted on polished cross sections to evaluate coatings' mechanical properties. The microhardness was assessed with a Vickers Leitz Wetzlar micro-hardness tester using a normal load of 100 g.

2.3 Corrosion Resistance Evaluation

Electrochemical impedance spectroscopy (EIS) measurements were carried out at room temperature (~ 22 °C) in a naturally aerated 3.5 wt% NaCl aqueous solution, according to the literature [44, 45]. Electrolyte 3.5% of sodium chloride was employed from one side to simulate aggressive envirnment containing chlorides that are the ions that create major problems of corrosion on aluminum alloys. Measurements were conducted after allowing the sample to stabilize at the open circuit potential (OCP) for 30 min. A standard three-electrode cell arrangement was used with the sample acting as the working electrode (1 cm^2), platinum as the counter electrode, and a saturated calomel reference electrode (SCE); all potentials are given with respect to the SCE. Electrochemical measurements were performed using potentiostat GAMRY Interface 1010E. A sinusoidal perturbation of 10 mV over the frequency range of 100 kHz to 0.1 Hz was applied. Impedance spectra were fitted to an appropriate electrical equivalent circuit (EEC) using Gamry Echem Analyst software. All the EIS tests were performed on the PEO-coated and uncoated specimens in triplicate to ensure repeatability.

Table 2 Chemical composition of glass additives

GLASS	SiO_2 wt%	Al_2O_3 wt%	B_2O_3 wt%	CaO wt%	SrO wt%	BaO wt%	Na_2O wt%	K_2O wt%	MgO wt%	Fe_2O_3 wt%
LCD	≥ 55.0	15.0	10.0	10.0	5.0	1.0	–	–	–	–
BS	72.0	7.0	12.0	1.0	–	< 0.1	6.0	2.0	–	–
SL	71.9	1.2	–	7.5	–	–	14.4	0.4	4.0	0.4

Local electrochemical properties were determined by scanning electrochemical microscopy (SECM) in 1 mM NaCl solution at room temperature. Before SECM testing, PEO-coated samples were embedded in epoxy resin. The Biologic M470 electrochemical workstation in dc-SECM mode was used for the measurements, and the scanned area of the sample was 300 × 300 µm with a step size of 10 µm. An ultramicroelectrode (UME) consisting of a 10 µm diameter Pt wire enclosed in glass was used as the working electrode, a Pt plate as the counter electrode, and an Ag/AgCl electrode as the reference electrode. The Pt UME was positioned at a constant height of 20 µm above the sample surface and scanned the area at a scan rate of 50 µm s^{-1}. Measurements were performed after 5 h of OCP stabilization. During the SECM testing, the tip current was recorded at each step over the area under investigation.

2.4 Wear Tests

Wear behaviour of PEO coatings was investigated by dry sliding wear tests in ambient conditions against a bearing steel. Thanks to their high strength-to-weight, Al alloys are often used for structural light weighting. Beyond the automotive sector, typical industrial applications of Al alloys such as AA6061 regard the packaging industry, where lightweighting of components allows higher productivity. In this field, aluminium parts are often involved in non-conformal line sliding contacts against a steel counterpart [46, 47]. Based on the above a slider-on-cylinder tribometer (block-on-ring contact geometry, ASTM G77) [48] was adopted: PEO-coated stationary blocks (6 × 6 × 70 mm^3) slid against a rotating cylinder made of the AISI 52100 bearing steel (40 mm diameter, 62 HRC hardness and surface roughness Ra = 0.1 µm). For all the dry sliding tests, total distance and linear speed were set at 1000 m and 0.3 m s^{-1}, respectively. Normal load ranged from 5 to 30 N, depending on the PEO layer wear resistance. Preliminary tests were conducted at 5 N for all samples, then normal load was increased every other test until the PEO layer was completely worn out. This procedure led to the identification of the load for coating failure for each PEO layer. The same configuration and testing conditions were also adopted for assessing the wear behavior of the uncoated AA6061 alloy that acted as a benchmark. Maximum contact pressures reported in Table 3 were evaluated by Hertzian theory [49] by considering elastic modulus and Poisson's ratio of the predominant phase in the PEO layer, being SiO_2 for layers obtained with direct current mode and both γ-Al2O3 and γ-AlO(OH) for pulsed ones as identified by XRD analyses.

During wear tests, normal and friction forces, as well as vertical displacement, were continuously monitored by the aid of load cells and a linear variable differential displacement transducer (LVDT). Therefore, friction coefficient and system wear (i.e. wear of both slider and cylinder) were dynamically recorded for the whole test duration. After tests, worn surfaces were characterized by 3D-digital (Hirox KH 7700) and SEM (Zeiss EVO 50, operating in low vacuum mode) microscopy, while maximum wear depth was measured by stylus profilometry on wear scars of sliders and cylinders.

3 Results and Discussion

3.1 Microstructural, Phase Composition and Mechanical Characterisation

SEM/EDS analysis were performed to determine the surface morphology and chemical composition of the prepared PEO coatings. Figure 1 shows the surfaces of the PEO coatings observed by SEM prepared in direct current mode, and Fig. 2 reports the surfaces of the PEO coatings prepared in pulsed current mode. All the micrographs indicate the presence of the pores and the pancake structure. The obtained microstructure is characteristic of PEO coatings on aluminium alloy [50, 51]. Porosity is formed by the melting of the oxide layer and the ejection of gas bubbles through discharge channels, and the discharge is created preferentially in relatively thin or faulty places, according to the literature [2, 52]. Pores of significantly larger sizes, on the order of 10 µm, are present in the samples prepared in direct current mode compared to those prepared in pulsed current mode, where the pores are 1–2 µm in size. Moreover, the distribution of pores in the PEO samples prepared by the pulsed mode is more homogeneous than in those prepared by the direct mode, which is in accordance with the literature where it is reported that coatings prepared by the direct current mode have limitations in controlling uniformity [53].

EDS analysis was performed on the surface of the PEO coatings, both for samples prepared in direct current mode

Table 3 Block-on-ring dry sliding wear tests (1000 m sliding distance, 0.3 m s^{-1} linear speed): maximum Hertzian contact pressures for PEO layers

Sample	Current mode	Maximum contact pressure (Mpa)				
		5 N	10 N	15 N	20 N	30 N
B-D, LCD-D, BS-D, SL-D	Direct	30	42	52	60	73
B-P, LCD-P, BS-P, SL-P	Pulsed	39	55	68	78	96
UNTREATED AA6061	–	30	43	52	61	74

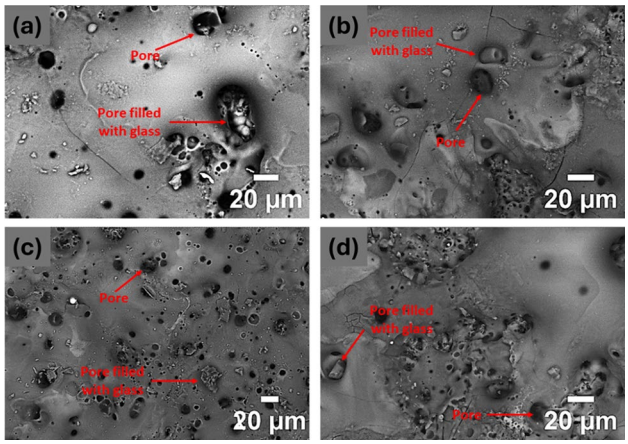

Fig. 1 SEM micrographs of the PEO-treated samples surface obtained by direct current mode with **a** no glass particle addition; **b** LCD glass; **c** BS glass; and **d** SL glass

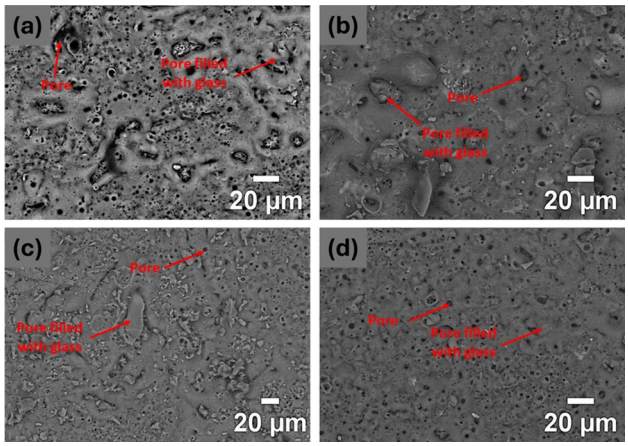

Fig. 2 SEM micrographs of the PEO-treated samples surface obtained by pulsed current mode with **a** no glass particle addition; **b** LCD glass; **c** BS; and **d** SL glass

and for samples prepared in pulsed current mode. The results are reported in Table 4. The main elements of the coatings are Al, coming from the substrate, and Si and Na, coming from the electrolyte solution. Compared to other samples, samples added with LCD glass particles show presence of calcium compunds. As calcium oxide is a component of LCD glass, this is to be expected. A certain concentration of Ca and Mg can also be found in samples where SL glass was added, confirming the presence of glass particles in the PEO coatings. Compared to the base coatings, no additional elements were detected in PEO samples with BS glass, but an increase in the concentration of the Si element can be seen (5.68% for samples prepared by direct current mode and 0.86% for samples prepared by pulsed current mode). In our previous research, Pezzato et al. [19], there was also an increase in the concentration of Si, which was evidence of the incorporation of BS glass into PEO coatings.

The results of cross-section SEM observation are shown in the micrographs in Fig. 3 for PEO coatings prepared by direct current mode and in Fig. 4 for coatings prepared by pulsed mode. Micrographs labeled A represent the base coatings, while B, C, and D show samples containing glass additives, LCD, BS, and SL glass, respectively. The black zone on the right side of the cross-section image indicates epoxy resin used for mounting samples.–The thickness of PEO coatings, measured by image analysis of SEM cross-section micrographs, is reported in Table 5. Direct current coatings are significantly thicker, approximately 100 µm, compared to pulsed coatings, which are approximately 10 µm in thickness. Moreover, glass particles did not affect thickness of the coatings. Instead, they were incorporated into the empty zones of the base coatings in both current regimes, which is consistent with our previous work [19]. The incorporation of glass particles is clearly visible on these micrographs, and it is marked by white circles, whereas the empty zones on the base coating are marked by red arrows. The melting point of glass additives (between 1000 and 1500 °C) is significantly lower than the working temperature of the PEO process, which is in the range of 1800–2370 °C [54]. The lower melting point of the glass additives may explain the inclusion of glass additives in the base coatings so that the glass quickly melts and resolidifies, forming an amorphous phase that partly seals the pores, as stated in our previous work [19] but also in the work of Fattah-alhosseini et al. [55]. They

Table 4 Semi-quantitative EDS results (wt%) obtained on PEO-coated samples with and without glass additives in both current regimes, direct and pulsed DC

Sample	O %	Na %	Si %	Al %	Ca %	Mg %
B-D	50.17	3.90	31.45	14.48	–	–
B-P	45.96	2.11	29.85	22.08	–	–
LCD-D	49.31	4.39	31.10	9.61	5.60	–
LCD-P	49.14	2.85	29.13	17.71	1.16	–
BS-D	51.06	2.46	37.13	9.39	–	–
BS-P	48.62	3.34	30.71	17.33	–	–
SL-D	49.53	6.31	30.24	9.80	2.78	1.35
SL-P	48.82	10.45	32.19	2.36	4.28	1.90

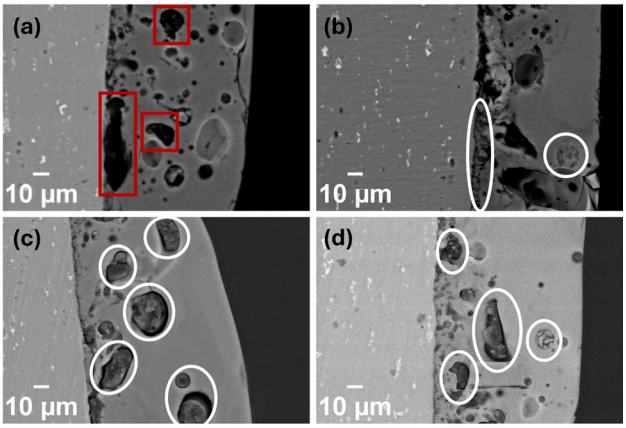

Fig. 3 SEM micrographs of the PEO-treated samples cross-section obtained by direct current mode with **a** no glass particle addition; **b** LCD glass; **c** BS glass; and **d** SL glass

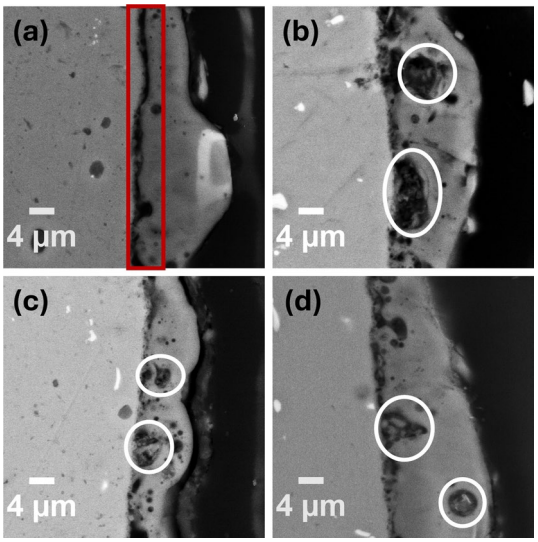

Fig. 4 SEM micrographs of the PEO-treated samples cross-section obtained by pulsed current mode with **a** no glass particle addition; **b** LCD glass; **c** BS glass; and **d** SL glass

also pointed out that particles having a high melting point, such as CeO_2 (2400 °C), SiC (2730 °C), and Si_3N_4 (1900 °C) were mostly incorporated inertly, disregarding their sizes.

Surface roughness parameters (Ra, Rq) are reported in Table 5. Considering that the base AA6061 alloy was polished before PEO and it was characterised by Ra and Rq equal to 0.4 ± 0.1 µm, all coatings resulted in a significant roughness increase. It is indeed well-known that PEO coatings are characterized by a high surface roughness due to the presence of pores and pancake structures, as also discussed previously. Overall, coatings obtained in pulsed mode were characterised by lower roughness than coatings processed with direct current. The result is supported by the analyses of the coating surface discussed in Figs. 1 and 2, that evidenced pores approximately one order of magnitude smaller in pulsed samples than in direct ones, with the smaller pores of pulsed samples being also more homogeneously distributed than in direct ones.

Generally, the addition of glass particles in the electrolyte induced an increase in the surface roughness. The effect of particle addition is more evident in samples obtained in pulsed mode, apart from BS-P glass that did not increase surface roughness if compared to the PEO layer without glass particles.

The microhardness $HV_{0,05/30}$ data are reported in Table 5. It is noticeable that the addition of glass particles significantly increases the microhardness of the coatings compared to the base coatings. The effect is more evident in samples with LCD glass particles. Microhardness is about 50% higher than in samples with SL glass and about 20% higher than in coatings with BS glass. This is also in agreement with the mechanical properties of the glasses, with the LCD glass being the one with the highest hardness. Considering this, it can be stated that the glass particles strongly influence the hardness of the obtained coatings.

Scratch tests carried out on PEO layers simulate the penetration of a singular asperity, allowing to assess the value of critical load related to the onset of coating failure (Lc2) and total coating breakthrough (Lc3). Samples obtained with pulsed mode, regardless of the type of electrolyte utilized in the PEO treatment, revealed comparable and very low values of both LC2 (approx. 2 N) and LC3 (approx. 4 N). On the other hand, samples processed with direct current revealed, with the exception of BS glass, quite higher critical loads, ranging from 8 to 25 N for Lc2 and from 12 to over 30 N for Lc3. As hardness is comparable between pulsed and direct samples, this result is most likely related to the lower coating thickness obtained by operating in pulsed mode. While the addition of glass particles did not affect the practical adhesion of the relatively thin pulsed samples, in the case of direct samples LCD glass particles, which also had the most beneficial influence on microhardness (Table 5), glass particles also succeeded in doubling the critical loads of the PEO coatings. On the other hand, the other types of glass additives were not beneficial. A similar ranking among PEO coatings was also evidenced by dry sling wear tests, discussed in the following sections.

The XRD diffraction patterns of PEO-coated samples in the presence and absence of glass particles are illustrated in Fig. 5 for coatings prepared by direct current mode and in Fig. 6 for coatings prepared by pulsed current mode. Strong diffraction peaks of the Al (ICSD 98-015-0692) coming from the substrate were identified in all the samples. XRD spectra show that the phase composition of the PEO coatings varies depending on the current regime used. When the direct current mode is used, mostly SiO_2

Table 5 Characterisation of PEO coatings: thickness, surface roughness, microhardness ($HV_{0.05/30}$), practical adhesion (LC2 and LC3 critical load from scratch tests), load for coating failure (from dry sliding wear tests)

Sample	Thickness (μm)	Roughness		Micro-hardness	Critical Load for coating adhesion (scratch tests)		Load for coating failure (wear tests)
		Ra (μm)	Rq (μm)	$HV_{0.05/30}$	LC2 (N)	LC3 (N)	Normal load (N)
B-D	71 ± 8	5.8 ± 0.6	7.6 ± 0.5	315 ± 0.6	12.1 ± 2.5	17.2 ± 0.5	20
B-P	11 ± 3	1.1 ± 0.1	1.5 ± 0.2	315 ± 1.5	2.3 ± 1.4	4.2 ± 0.9	10
LCD-D	70 ± 3	6.6 ± 0.5	8.8 ± 0.8	898 ± 1.0	25.4 ± 3.9	> 30	30
LCD-P	11 ± 2	5.3 ± 1.7	8.3 ± 2.3	898 ± 0.6	2.4 ± 1.3	3.8 ± 1.2	10
BS-D	82 ± 11	6.6 ± 0.4	10.3 ± 1.1	701 ± 2.3	3.5 ± 0.7	5.2 ± 0.1	15
BS-P	7 ± 2	1.0 ± 0.1	1.3 ± 0.1	701 ± 0.0	1.7 ± 0.2	3.6 ± 0.9	5
SL-D	81 ± 3	7.9 ± 1.2	10.0 ± 1.5	418 ± 1.5	8.3 ± 0.1	11.9 ± 1.2	20
SL-P	13 ± 3	3.0 ± 1.3	5.0 ± 2.5	418 ± 2.0	1.7 ± 0.1	3.2 ± 0.3	5

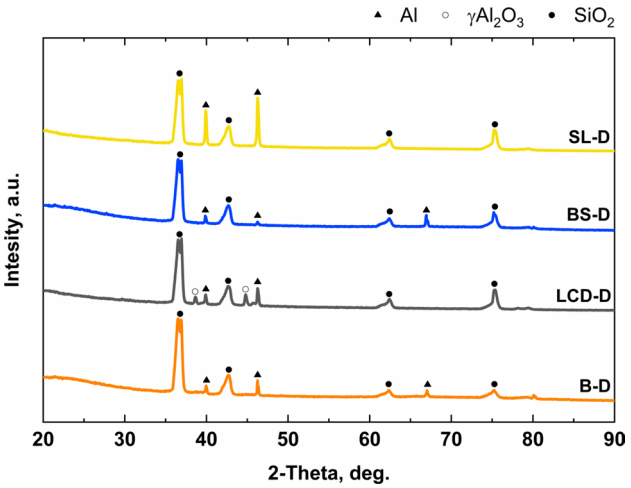

Fig. 5 X-ray diffraction patterns of the PEO treated samples obtained with direct current mode

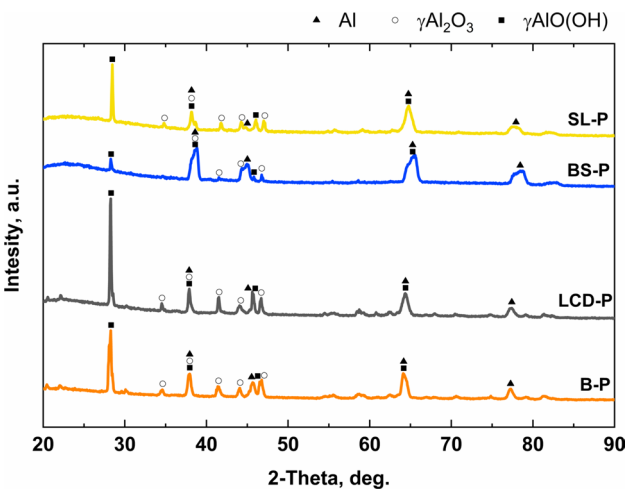

Fig. 6 X-ray diffraction patterns of the PEO treated samples obtained with pulsed current mode

(ICSD 98-018-1307) is formed and traces of γ-Al_2O_3 (ICSD 98-017-3014) can be found. Otherwise, SiO_2 is not found in the coatings prepared by the pulsed current mode, but only the diffraction peaks of the aluminum compounds can be seen, γ-Al_2O_3 (ICSD 98-017-3014) and γ-AlO(OH) (ICSD 98-002-7865). This particular behavior between direct and pulsed current mode, when a silicate base solution is used, is in accordance with the fact that in direct current mode more strong discharge phenomena that persist longer over the processed surface occur in comparison to pulsed current mode. Due to this fact the electrolyte remain trapped into the discherge channel for longer time in the direct current mode, thus permitting the formation of higher amount of silcon oxide wich derives from the electrolyte. Diffraction peaks of glass additives were not found in the XRD spectra, suggesting that are located in the amorphous part of the spectrum, as already reported in the literature [19]. Comparing the results of the XRD analysis with the results of the EDS (Table 4) permit clearly to evidence the absence in the XRD spectra of Ca and Mg compounds, that come only from the glass, and are probably present in the coating only as an amorphous phase. Also, Na compounds are not present in the XRD spectra. Na compounds come both from the glass and from the electrolyte, the part from the glass is present probably as amorphous phase whereas the part coming from the electrolyte is below the detection limit of the XRD.

3.2 Corrosion Resistance Evaluation

The corrosion resistance of PEO coatings was studied using EIS. Comparison between samples with and without glass additives in PEO coatings was made during two different current modes of PEO, pulsed and direct. In many cases, this electrochemical technique has been used to analyze the corrosion resistance of PEO coatings in a 3.5% NaCl electrolyte which simulates a corrosive chloride environment [56]. The experimental results are shown in the form of Nyquist plots,

Fig. 7 and Bode plots, Fig. 8. The Bode plot representation is presented in the form of Bode Modulus plots and Bode Phase plots. In the figures, indication (a) refers to samples prepared by direct mode, while indication (b) refers to samples prepared by pulsed mode.

To determine quantitative electrochemical parameters of the phenomenon taking place during exposure to the electrolyte, EIS data are commonly analysed by fitting it to an EEC [57]. In EEC, different electrical elements are used to represent the charge's path through the system components.

The EIS data were fitted using three different EEC models, all shown in Fig. 9. In the EECs, a constant phase element (CPE) instead of a capacitance was used, since often the coating does not behave as a pure capacitance because the electrical properties of the material are not constant through the thickness. Then, the measured phase angle at high frequency is not equal to − 90°, which can be seen in the EIS results shown in the form of Bode Phase plots in Fig. 8, where it is noticeable that none of the curves has a value of -90° that would indicate an ideal capacitor [58]. The impedance of a CPE can be expressed by the following equation:

$$Z_{CPE} = \frac{1}{Y(j\omega)^a}$$

j is the imaginary unit, Y is the constant phase element, a is an empirical exponent, and ω is the angular frequency of the sine wave defined as:

$$\omega = 2\pi f$$

where f is the frequency. The empirical exponent a represents the physical meaning of the CPE and can assume the value of 1 in the case of a perfect capacitor, and 0 in the case of a perfect resistor. Deviations of a from these values indicates the non-ideality of the system. If the value of the exponent a is approximately 1, Y is similar to a pure capacitor and can be considered:

$$C = \frac{\varepsilon_0 \varepsilon A}{d}$$

where C is the capacitance, ε_0 is the permittivity of vacuum, ε is the dielectric constant, A is the effective area, and d is the thickness of the layer [59] [NO_PRINTED_FORM] [60].

Accordingly, the aluminium substrate is fitted with a simple EEC (Fig. 9a), consisting of one resistive element (R_o) added in parallel to one capacitive element (CPE_o) representing an oxide layer on the bare aluminium alloy.

PEO coatings usually consist of two layers, an outer porous layer and an inner barrier layer [61]. The Phase Bode plot for the PEO-coated samples with and without glass additives, Fig. 8, demonstrates two-time constants which represent the resistance offered by the outer porous layer and inner barrier layer, respectively. The high-frequency semi-circle demonstrates the outer layer properties, whereas the low-frequency semi-circle demonstrates the inner barrier layer properties [62]. On the other hand, bare aluminium alloy has only one time constant, indicating that corrosion protection is given only by the oxide layer.

Therefore, the EECs that can best fit the experimental data, shown in Fig. 9b, contain R_p and CPE_p related to the external porous layer and R_b and CPE_b that represent the polarisation resistance and constant phase element of the inner barrier layer, respectively. R_s represents the resistance of the electrolyte, and it is presented in all the EEC. The value of R_s depends primarily on the electrochemical cell's geometry and the test solution's conductivity. The values

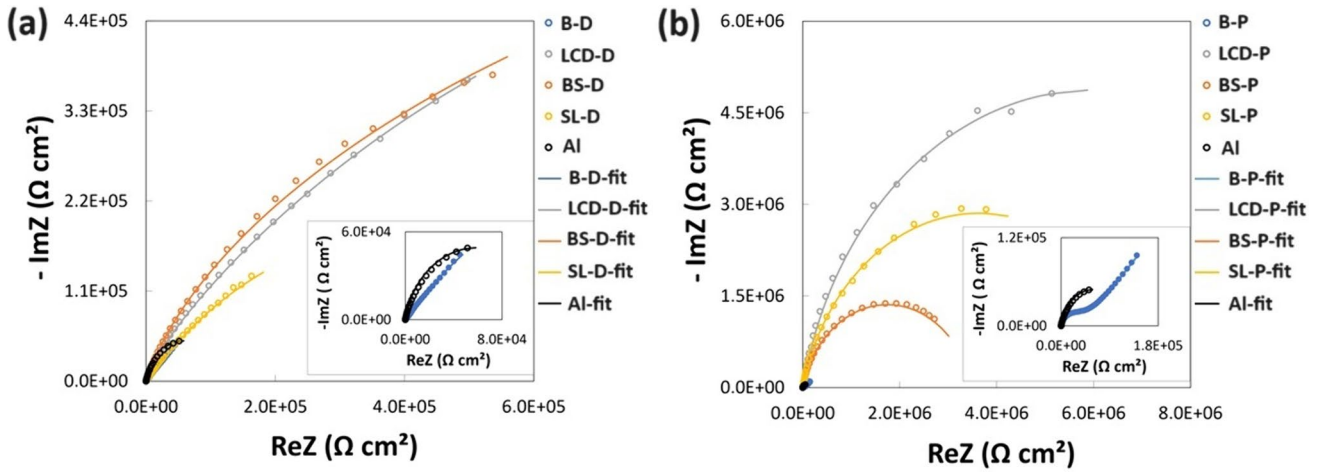

Fig. 7 Experimental results of EIS tests in terms of Nyquist plots and results of fitting experimental results with EEC (shown as lines) for the: **a** PEO coatings prepared by direct current mode and **b** PEO coatings prepared by pulsed current mode

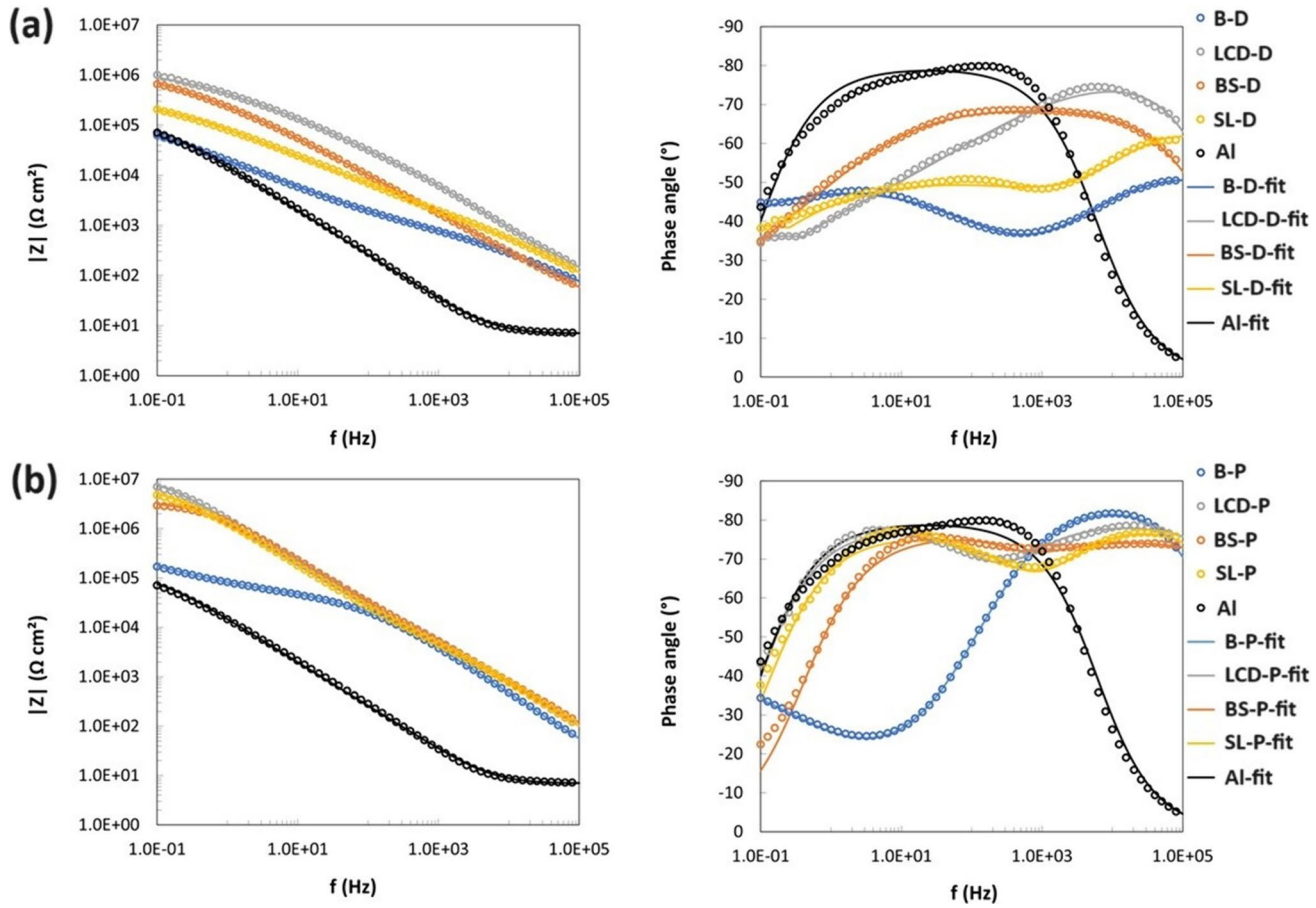

Fig. 8 Experimental results of EIS tests in terms of Bode plots and results of fitting experimental results with EEC (shown as lines) for the: **a** PEO coatings prepared by direct current mode and **b** PEO coatings prepared by pulsed current mode

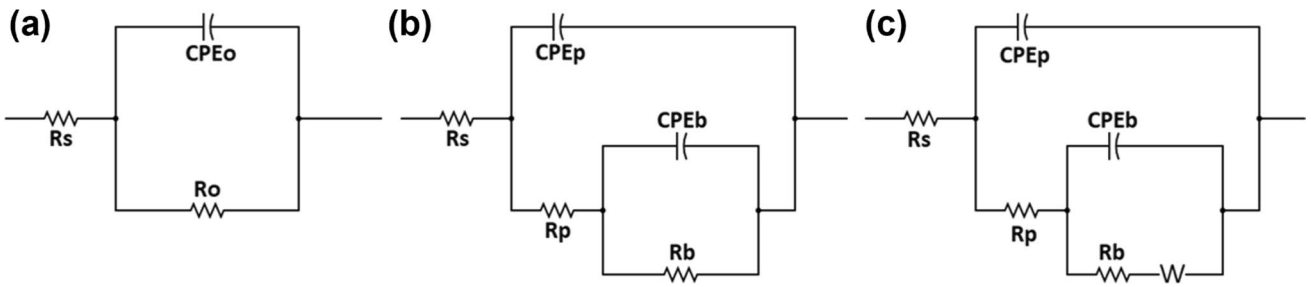

Fig. 9 Equivalent Electrical Circuits (EECs) employed for curve fitting of **a** untreated sample and **b** PEO-treated samples **c** with Warburg element

obtained from the fitted spectra were consistently small, between 4.1 and 32.8 Ω cm^2 (see Tables 6 and 7).

Different behaviour of the impedance curves at the low-frequency regions was observed, in the sample without the glass additives prepared by Pulsed DC mode. Therefore this sample is fitted with the EEC shown in Fig. 9c. The EEC is the same as the one before, with an additional Warburg element added in series with R_b. This means that the corrosion process is mostly diffusion controlled, as evidenced by the increase of the Nyquist curve at low frequencies, Fig. 7b. That behaviour is caused by the empty pores in PEO coating without the glass additives, which may allow corrosive electrolytes to diffuse into them, and it is in good agreement with the SEM cross-section micrograph (Fig. 4a).

Table 6 Fitting results of the experimental EIS data for the samples prepared by the direct current mode and bare aluminium substrate

	Sample				
	Untreated	B-D	LCD-D	BS-D	SL-D
χ^2	4.9×10^{-3}	1.8×10^{-4}	1.9×10^{-3}	3.3×10^{-4}	4.0×10^{-4}
R_s (Ω cm^2)	6.9	4.2	32.8	12.7	8.7
R_o (Ω cm^2)	1.2×10^{5}	–	–	–	–
Y_o (F cm^{-2} Hz^{1-a})	1.3×10^{-7}	–	–	–	–
a_o	0.88	–	–	–	–
R_b (Ω cm^2)	–	4.2×10^{5}	1.6×10^{6}	1.7×10^{6}	6.1×10^{5}
Y_b (F cm^{-2} Hz^{1-a})	–	1.4×10^{-5}	6.9×10^{-7}	6.1×10^{-7}	3.8×10^{-6}
a_b	–	0.42	0.49	0.78	0.40
R_p (Ω cm^2)	–	1.1×10^{3}	2.0×10^{4}	6.3×10^{1}	1.2×10^{3}
Y_p (F cm^{-2} Hz^{1-a})	–	3.1×10^{-6}	8.6×10^{-8}	7.5×10^{-7}	2.7×10^{-7}
a_p	–	0.62	0.85	0.37	0.78

Results of the fitting of the experimental data from the EIS test with the EECs are reported in Table 6 for the samples prepared by direct current mode and Table 7 for the samples prepared by pulsed mode. The fitting results of the bare aluminium substrate are shown in both tables for comparison.

The quality of the fittings was evaluated based on the chi-squared values and the strong agreement between experimental plots, in form of circles, and fitting plots in form of lines. Chi-squared values is the square of the standard deviation between the original data and the calculated spectrum. The lower the values, the better the fitting [60]. The values were in the range 4.9×10^{-3} – 6.0×10^{-5} indicating good agreement between the experimental data and equivalent circuit fits (see Tables 6 and 7).

Table 7 Fitting results of the experimental EIS data for the samples prepared by the pulsed current mode and bare aluminum substrate

	Sample				
	Untreated	B-P	LCD-P	BS-P	SL-P
χ^2	4.9×10^{-3}	6.0×10^{-5}	8.6×10^{-4}	1.4×10^{-3}	1.5×10^{-3}
R_s (Ω cm^2)	6.9	14.1	6.0	4.1	8.8
R_o (Ω cm^2)	1.2×10^{5}	–	–	–	–
Y_o (F cm^{-2} Hz^{1-a})	1.3×10^{-7}	–	–	–	–
a_o	0.88	–	–	–	–
R_b (Ω cm^2)	–	5.8×10^{4}	1.2×10^{7}	3.4×10^{6}	7.3×10^{6}
Y_b (F cm^{-2} Hz^{1-a})	–	2.0×10^{-6}	4.9×10^{-8}	5.9×10^{-9}	9.2×10^{-8}
a_b	–	0.48	0.86	0.98	0.82
R_p (Ω cm^2)	–	1.2×10^{4}	4.1×10^{4}	5.9×10^{4}	1.1×10^{4}
Y_p (F cm^{-2} Hz^{1-a})	–	6.2×10^{-8}	7.9×10^{-8}	1.3×10^{-7}	7.4×10^{-8}
a_p	–	0.94	0.88	0.83	0.88
W (F cm^{-2} Hz^{1-a})	–	6.9×10^{-6}	–	–	–

Based on the data in the Tables 6 and 7, it is apparent that the corrosion resistance is improved with glass particles added to the PEO samples, that are showing the highest R_p and R_b values. Results are consistent with the literature, which suggests that pore sealing in PEO coatings improves corrosion resistance [63].

Generally, the internal barrier layer, in all PEO-treated samples, provides corrosion resistance, due to its higher value of polarization resistance than the outer porous layer, which is in accordance with literature data for PEO coatings [62]. Additionally, a lower value of Y indicates more compact layer [62, 64], and all PEO coatings with glass additives have lower values of Y compared to coatings without glass additives. A lower value of Y is present in both layers of the PEO coating, the barrier and the porous one. This result agreed well with the SEM observation of cross-sections, Figs. 3 and 4, where pore sealing is clearly visible in the samples with glass additives.

In comparison with the other coatings, LCD-P stands out as the sample with the highest corrosion resistance, with an R_b value of 1.2×10^{7} Ω cm^2, (two order of magnitude, 9900% of improvement in comparison with the untreated sample) which is one order of magnitude higher than the next best coating.

Moreover, pulsed samples with glass particles possess R_b values ranging from 3.4×10^{6} Ω cm^2 for the BS-P sample (2733% of improvement in comparison to the untreated AA) to 1.2×10^{7} Ω cm^2 for the LCD-P sample, up to two orders of magnitude higher than those prepared by direct mode, whose values range from 6.1×10^{5} Ω cm^2 for the SL-D sample (408% of improvement in comparison to the untreated) to 1.7×10^{6} Ω cm^2 for the BS-D sample (1316% of improvement in comparison to the untread). Compared to direct, pulsed samples have a higher corrosion resistance due to their more homogenous PEO coating structures and smaller pores [28]. In this way, the pores are more likely to be filled with glass particles, reducing the possibility of free spaces within the coating.

Summarizing, considering the corrosion properties of the coated samples and comparing the value of R_b of the samples with PEO coatings to the value of R_o of the uncoated sample the following percentage of improvement of the corrosion resistance can be calculated: B-D 250%; LCD-D 1233%; BS-D 1316%; SL-D 408%; B-P -51%; LCD-P 9900%; BS-P 2733%; SL-P 5983%. Considering these results resulted clear that all the coatings containing glass particles produce remarkable improvement in the corrosion properties and that generally the layers produced in pulsed mode behave better

that the ones obtained in DC mode. Considering the different types of glasses LCD glass seem the most promising in improving the corrosion performances of PEO coatings.

The distinct corrosion behaviors observed in PEO coatings with various glass additives align with the concentration of alkaline elements within the glass's chemical composition. Best outcomes were observed in LCD samples, characterized by alkali-free glass, while results with BS and SL glass varied based on the current regime of the PEO process. In corrosive conditions, alkaline elements have the potential to leach out of the glass structure, creating vacancies subsequently filled by water molecules. The principle of preferential leaching relies on the thermodynamic and kinetic stability of distinct glass modifiers. At lower temperatures and for ions with the same charge, the diffusion of larger ions becomes energetically unfavorable, while smaller ions can move more easily through the glass network. Typically, double-charged ions (alkaline earth elements) tend to exhibit lower diffusivity within the glass network compared to single-charged ions (alkaline elements). This difference primarily arises due to the pronounced influence of highly intense local electric fields acting on the double-charged ions.

Moreover, the substitution of high-radius cations like K^+ from the bulk creates larger voids in the glass network compared to the substitution of smaller cations like Na^+, thereby facilitating the penetration of water molecules into deeper regions. While all alkaline silicate glass are prone to degradation, their stability, from a thermodynamic perspective, tends to increase in the following order: $K_2SiO_3 < Na_2SiO_3 < Li_2SiO_3$ [40]. The high corrosion resistance obtained in the sample with the addition of LCD glass can also be related to the fact that this glass is a "shorter" glass in comparison to BS and SL glasses thank to the absence of alkali. Due to this fact, during the PEO treatment, the LCD glass can soften more than the other thus better filling the pores and producing a higher barrier effect against the external environment.

The most promising samples according to the EIS results, LCD-D and LCD-P, were further analysed by the SECM method in 1 mM NaCl. When comparing the current maps (Fig. 10) recorded over the surface of the measured samples, differences can be seen. For the LCD-D sample (Fig. 10a), the current distribution is more or less uniform over the entire surface, and only positive currents related to the dissolution of the coating were detected. The situation is somewhat different for sample LCD-P, where the maximum positive current is higher than for LCD-D. Although higher current is indicating more intense dissolution at these sites, it should be noted that this maximum is strictly localised and the rest of the sample shows positive current values comparable to those of the direct curret counterpart. On the other hand, negative current values were observed in the LCD-P sample, indicating the presence of cathodes on the examined area. This could be directly attributed to the detection of base aluminium alloys due to the lower thickness of the LCD-P coating (11 vs. 70 µm). Localised electrochemical investigation of the samples showed a different behaviour than the EIS investigation, which can be attributed to the fact that the samples were exposed to the aqueous solution for a longer time and solution was able to penetrate the base material through the thinner LCD-P coating.

3.3 Wear Behaviour

As regards block-on-ring dry sliding wear tests, samples were tested at increasing normal load up to coating failure, occurred at different loads as reported in Table 5. Pulsed

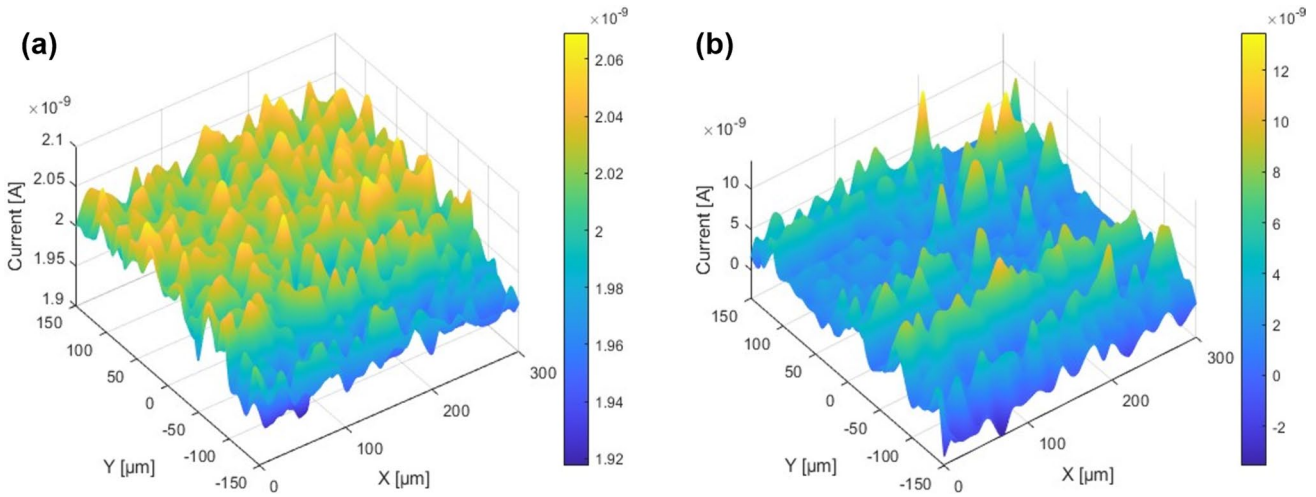

Fig. 10 Results of SECM measurements of the **a** LCD-D and **b** LCD-P samples in 1 mM NaCl

layers, whose thickness was significantly lower than direct ones, survived at a maximum of 10 N load while direct samples were tested up to 30 N load.

Results of wear tests, in terms of steady-state coefficient of friction (COF) and maximum wear depth measured on sliders, are reported in Figs. 11 and 12. Wear depth of the steel counterpart was also taken into consideration but, regardless the applied normal load or the type of PEO layer, it was always non-detectable. Steady-state COF was evaluated, starting from dynamic acquisition during test, as average value after the run-in distance, set at 300 m. It is worth recalling that COF is the result of two different contributions: adhesive and abrasive. PEO layers, by reason of the increase in both hardness and roughness, usually raise the abrasive contribution and, therefore, by comparison to the untreated alloy, they induce an increase in the COF. However, by focusing on Fig. 11, in the present study this condition occurs only at high normal loads for PEO direct layers. Otherwise, by considering also standard deviations, COF of untreated alloy was higher or at least comparable to

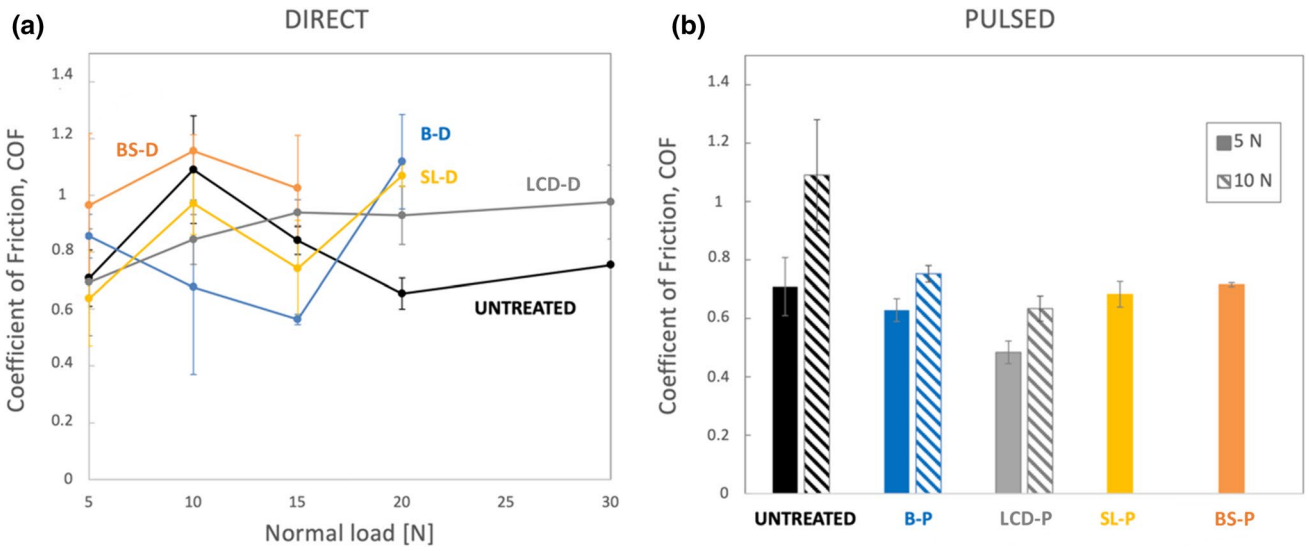

Fig. 11 Results of block-on-ring dry sliding wear tests (1000 m sliding distance, 0.3 m s^{-1} linear speed): steady-state coefficient of friction of **a** direct and **b** pulsed samples compared to untreated alloy

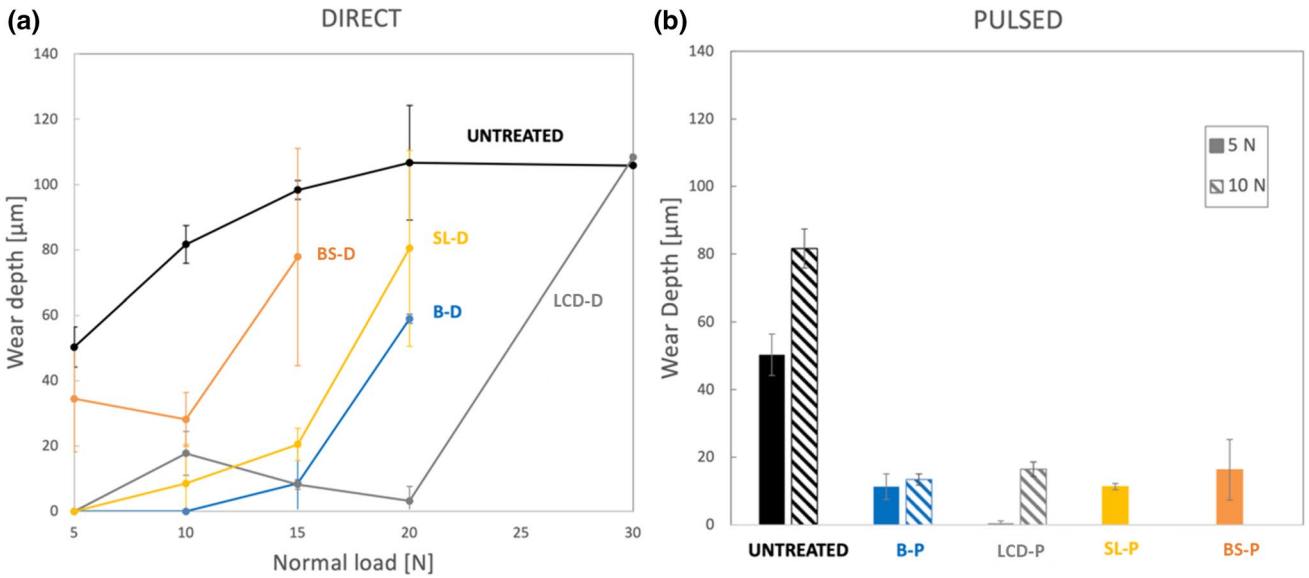

Fig. 12 Results of block-on-ring dry sliding wear tests (1000 m sliding distance, 0.3 m s^{-1} linear speed): maximum wear depth on sliders of **a** direct and **b** pulsed samples compared to untreated alloy

the PEO-treated one. By referring to the analyses of the wear scars in Figs. 13, 14 and 15, discussed in the following, this instance can be explained considering: (1) the severe adhesion wear experienced by the untreated alloy that enhanced the adhesion component of COF; (2) instability at the asperities of the PEO due to microcracking phenomena and the establishment of a protective oxidative tribo-layer between contact surfaces that limited the rise of the abrasive component of COF. Generally, the addition of glass particles induced an increase of the COF of the PEO layers, because of the increase of both surface roughness and hardness (see Table 5), with the only exception of LCD-P samples. On the other hand, all PEO layers induced a significant increase in the wear resistance, by reducing up to one order of magnitude the wear depth if compared to the untreated alloy. Among the glass particles used as additives, LCD ones maximized wear resistance of both pulsed and direct samples. By contrast, the addition of SL and BS glass in the PEO layer did not exert a beneficial effect in the wear resistance. As concerns load for coating failure (see Table 5), LCD samples showed the greatest one in both direct and pulsed configuration. In particular, in case of direct samples, LCD-D was the only layer to survive up to a 30 N load, also improving the wear resistance of PEO layers without additives (B-D). For pulsed samples, instead, LCD-P survived up to 10 N load with a wear resistance comparable to the base PEO (B-P samples). The improved tribological properties obtained with the addition of the LCD glass can be on the one hand related to the best sealing of the pores obtained with this glass (due to the fact that it is "shorter" in comparison to the other glasses, as previously discussed), and on the other hand to the higher mechanical properties (Table 5) conferred by this glass to the PEO coating.

Figures 13, 14 and 15 compares wear scars morphology of samples after 5 N tests. From Fig. 13 an overall view of wear scars is proposed for all tested samples, observed with a 3D digital optical microscope, while high-magnification detailed SEM analyses are reported in Figs. 14 and 15 for a representative set of samples, being: untreated alloy, base PEO, PEO with additive exhibiting the best and the worst tribological performance. For SEM analyses, back scattered electrons (BSE) images are proposed for the characterization at the edges of wear scars, to underline the formation and distribution of oxide-based layers, while secondary electrons (SE) images, enhancing morphological features, are proposed for the center of wear scars. Wear scars morphology in Fig. 13 show that the untreated alloy suffered severe adhesion phenomena, as shown also by the images in Fig. 14a, b. Plastic deformation dominates wear scars of untreated alloy, characterized by the presence of long and continuous grooves due to ploughing (highlighted by dashed green circles in Fig. 14b). On the other hand, scars of PEO layers who survived the tests are characterized by a tribolayer that appears reddish in the micrographs of Fig. 13 and bright

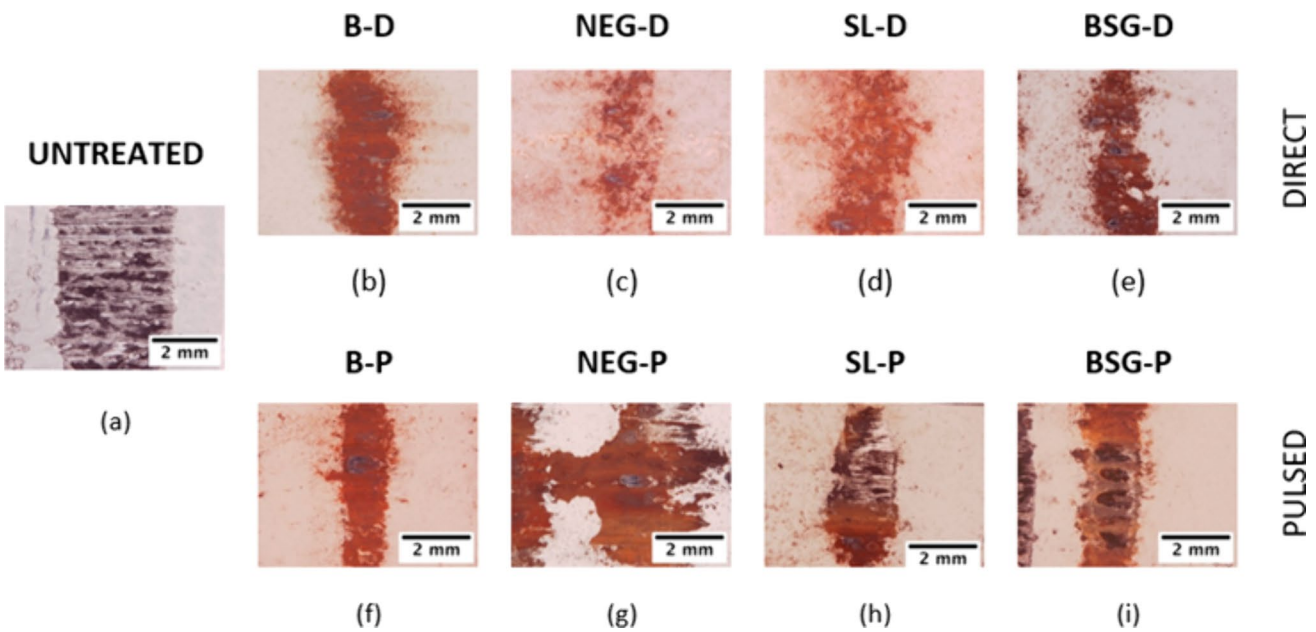

Fig. 13 Overview of wear scars morphology for all samples subjected to block-on-ring dry sliding wear tests with 5 N load (1000 m sliding distance, 0.3 m s^{-1} linear speed): **a** untreated alloy; **b** PEO obtained in direct mode without additives, **c** PEO obtained in direct mode with LCD particles, **d** PEO obtained in direct mode with SL particles; **e** PEO obtained in direct mode with BS particles; **f** PEO obtained in pulsed mode without additives, **g** PEO obtained in pulsed mode with LCD particles, **h** PEO obtained in pulsed mode with SL particles; **i** PEO obtained in pulsed mode with BS particles

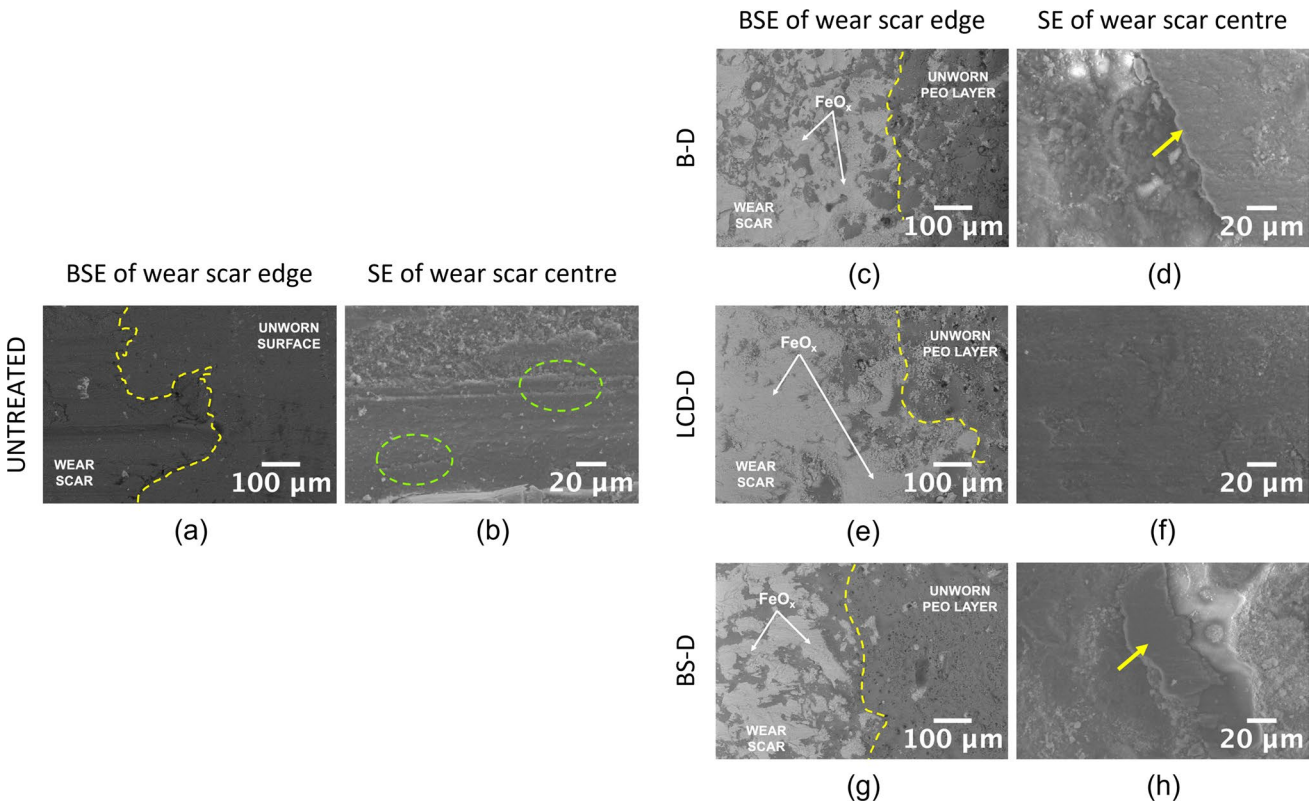

Fig. 14 Characterization of wear scars with scanning electron microscopy (back scattered electrons are used for the edge and secondary electrons for the center of scars) for selected samples subjected to block-on-ring dry sliding wear tests with 5 N load (1000 m sliding distance, 0.3 m s^{-1} linear speed): **a**, **b** untreated alloy; **c**, **d** PEO obtained in direct mode without additives; **e**, **f** PEO obtained in direct mode with LCD particles; **g**, **h** PEO obtained in direct mode with BS particles; The yellow dashed lines in BSE images define the edge of wear scars while basic geometric shapes in SE images underline damaging phenomena of surfaces discussed in the text

grey in Figs. 14 and 15 (BSE images). The tribolayer is the results of the tribological contact with the steel counter face and consist of Fe-based oxides, as already observed in a previous work [65] and confirmed by EDS analyses. Such oxide-based tribolayer has a protective function, therefore it leads to a mild wear regime, as also demonstrated by the low wear depth measured on sliders (Fig. 12). However, it is worth recalling that wear depth of the steel counterpart was always non detectable. SEM analyses in Figs. 14 and 15 evidenced that the protective oxide layer was thicker and more continuous in case of LCD samples, obtained with both direct and pulsed configuration (Figs. 14e and 15c), supporting the negligible wear depth discussed in Fig. 12. The high magnification analyses of scar center also showed that LCD-P suffered of a minor micro-cracking phenomenon (highlighted by orange arrows in Fig. 15d), while no micro cracks are evidenced in LCD-D. Conversely, protective layers formed on the other samples were less dense and compact, especially in case of BS ones (Figs. 14g and 15e), and the detailed analyses of scars morphology evidenced the presence of several discontinuities in the protective tribolayer, thus justifying the worse wear resistance of B and BS samples than LCD ones. Such discontinuities can be synthetized as a more marked microcracking (underlined by orange arrows in Fig. 15f), eventually leading to fragmentation of the oxide layer, evidenced by the large and compacted fragments (indicated by yellow arrows in Fig. 14d, h), and the formation of debris retained in the worn surface (highlighted by the dashed line orange circle in Fig. 15b).

4 Conclusions

The main conclusions that can be drawn from the present work can be summarized as follows:

- Three different types of glass (LCD, BS and SL) were successfully incorporated into PEO coatings produced on the 6061 wrought aluminium alloy.
- The incorporation mechanism resulted partially reactive with melting and re-solidification of the glass particles during the PEO process, with the glass that fill the pores of the PEO layer.

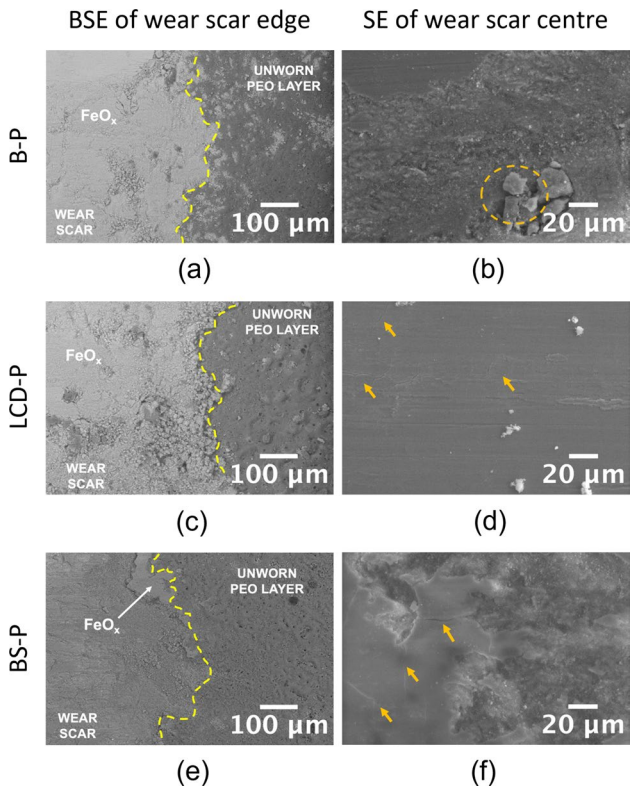

Fig. 15 Characterization of wear scars with scanning electron microscopy (back scattered electrons are used for the edge and secondary electrons for the center of scars) for selected samples subjected to block-on-ring dry sliding wear tests with 5 N load (1000 m sliding distance, 0.3 m s^{-1} linear speed): **a**, **b** PEO obtained in pulsed mode without additives, **c**, **d** PEO obtained in pulsed mode with LCD particles; **e**, **f** PEO obtained in pulsed mode with BS particles. The yellow dashed lines in BSE images define the edge of wear scars while basic geometric shapes in SE images underline damaging phenomena of surfaces discussed in the text

- The morphology of the coating is strongly influenced by the current mode. DC mode produce thicker coatings whereas PC mode produce thinner but more compact layers.
- The capacity of the glass to seal the pores strongly depends by the type of the glass. The main difference in the three glasses is the alkali content that produce a strong modification in the thermal, mechanical, and corrosion properties. The glass that is more able to fill the pores of the PEO layer is the LCD glass which is characterized by a smaller difference between transition temperature and softening temperature due to the absence of alkaline elements.
- Considering the corrosion properties, EIS tests showed in all the cases that the addition of glass particles improves the corrosion resistance, thank to the sealing of the pores. The corrosion resistance was higher in the samples obtained in PC mode, thank to the higher compacteness. The best additive was the LCD glass, thanks to its better ability ito seal the pores as well as its higher chemical stability, conferred by the absence of the alkaline elements.
- Localized corrosion tests confirmed that the best additive is the LCD glass but also showed that the samples obtained in DC mode are more promising when exposed to an aggressive environment for a prolonged time.
- Considering the tribological behaviour, the LCD glass produces an increase in tribological performance, whereas the other glasses are not beneficial. This behaviour can be ascribed to the better ability of this glass to sealing the pores and induce higher mechanical properties.

Author Contribution Luca Pezzato: Investigation, Formal analysis, Data Curation, Writing—Original Draft, Conceptualization, Methodology, Validation, Writing—Review & Editing, Supervision Lorena Kostelac: Investigation, Formal analysis, Data Curation, Writing—Original Draft, Visualization, Writing—Review & Editing Lavinia Tonelli: Investigation, Formal analysis, Data Curation, Visualization, Writing—Original Draft, Writing—Review & Editing Hamada Elsayed: Investigation, Writing—Review & Editing Daniel Kajánek: Investigation, Writing—Original Draft, Writing—Review & Editing Enrico Bernardo: Validation, Writing—Review & Editing, supervision Carla Martini: Validation, Writing—Review & Editing, supervision Manuele Dabalà: Validation, supervision, Funding Acquisition Katya Brunelli: Validation, Writing—Review & Editing, supervision, Funding Acquisition.

Funding Open access funding provided by Università degli Studi di Padova within the CRUI-CARE Agreement. This research was supported by Science Grant Agency of the Slovak Republic through project No. 1/0153/21.

Declarations

Conflict of interest The authors declare that they have no known competing financial interests or personal relationships that could have appeared to influence the work reported in this paper.

References

1. C. Premchand, P. Manojkumar, E. Lokeshkumar, L. Rama Krishna, B. Ravisankar, N. Rameshbabu, Surf. Coat. Technol. **449**, 128975 (2022). https://doi.org/10.1016/j.surfcoat.2022.128975
2. P. Van Truong, N. Van Bo, N. Van Minh, N. Viet Anh, G. Suresh Kumar, M. Shkir, Mater. Chem. Phys. **290**, 126587 (2022). https://doi.org/10.1016/j.matchemphys.2022.126587
3. M. Sowa, A. Olesiński, B. Szumski, A. Maciej, M. Bik, P. Jeleń, M. Sitarz, W. Simka, Electrochim. Acta **424**, 140652 (2022). https://doi.org/10.1016/j.electacta.2022.140652
4. M. Hashemzadeh, K. Raeissi, F. Ashrafizadeh, A. Hakimizad, M. Santamaria, T. Lampke, Coatings **12**(1), 33 (2022). https://doi.org/10.3390/coatings12010033
5. K. Babaei, A. Fattah-alhosseini, M. Molaei, Surf. Interfaces **21**, 100677 (2020). https://doi.org/10.1016/j.surfin.2020.100677
6. R. Wang, J. Zhou, Mater. Res. Express **6**, 086566 (2019). https://doi.org/10.1088/2053-1591/ab1a14
7. S. Gowtham, T. Arunnellaiappan, N. Rameshbabu, Surf. Coat. Technol. **301**, 63–73 (2016). https://doi.org/10.1016/j.surfcoat.2016.02.043
8. J.S. Santos, V. Márquez, J.G. Buijnsters, S. Praserthdam, P. Praserthdam, Appl. Surf. Sci. **607**, 155072 (2023). https://doi.org/10.1016/j.apsusc.2022.155072
9. M. Asgari, H. Daneshmand, G. Bratai Darband, A.S. Rouhaghdam, Surf. Interfaces **21**, 100712 (2020). https://doi.org/10.1016/j.surfin.2020.100712
10. Z. Ye, D. Liu, C. Li, X. Zhang, Z. Yang, M. Lei, Acta Metall. Sin. (Engl. Lett.) **27**(4), 705–713 (2014). https://doi.org/10.1007/s40195-014-0104-9
11. V. Hutsaylyuk, M. Student, V. Posuvailo, O. Student, Y. Sirak, V. Hvozdets'kyi, P. Maruschak, H. Veselivska, Vacuum **179**, 109514 (2020). https://doi.org/10.1016/j.vacuum.2020.109514
12. X. Lu, C. Blawert, M.L. Zheludkevich, K.U. Kainer, Corros. Sci. **101**, 201–207 (2015). https://doi.org/10.1016/j.corsci.2015.09.016
13. A.A. Chirkunov, A.G. Rakoch, E.V. Monakhova, A.A. Gladkova, Z.V. Khabibullina, V.A. Ogorodnikova, M. Serdechnova, C. Blawert, Y.I. Kuznetsov, M.L. Zheludkevich, Int. J. Corros. Scale Inhib. **8**, 1170–1188 (2019). https://doi.org/10.17675/2305-6894-2019-8-4-22
14. J. Liu, X. Huang, Y. Ren, L.M. Wong, H. Liu, S. Wang, Sci. Rep. **12**, 4532 (2022). https://doi.org/10.1038/s41598-022-08727-7
15. X. Lu, M. Mohedano, C. Blawert, E. Matykina, R. Arrabal, K.U. Kainer, M.L. Zheludkevich, Surf. Coat. Technol. **307**, 1165–1182 (2016). https://doi.org/10.1016/j.surfcoat.2016.08.055
16. J. Lu, X. He, H. Li, R. Song, Materials **11**(7), 1062 (2018). https://doi.org/10.3390/ma11071062
17. M. Rizwan, R. Alias, U.Z. Zaidi, R. Mahmoodian, M. Hamdi, J. Biomed. Mater. Res. Part A **106A**, 590–605 (2018). https://doi.org/10.1002/jbm.a.36259
18. T. Kikuchi, T. Taniguchi, R.O. Suzuki, S. Natsui, Thin Solid Films **697**, 137799 (2020). https://doi.org/10.1016/j.tsf.2020.137799
19. L. Pezzato, L. Lorenzetti, L. Tonelli, G. Bragaggia, M. Dabalà, C. Martini, K. Brunelli, Surf. Coat. Technol. **428**, 127901 (2021). https://doi.org/10.1016/j.surfcoat.2021.127901
20. Y. Li, C. Guo, C. Qi, D. Zhang, H. Sun, S. Yang, Y. Wan, Y. Wang, Prog. Org. Coat. **192**, 108495 (2024). https://doi.org/10.1016/j.porgcoat.2024.108495
21. E. Erfanifar, M. Aliofkhazraei, H. Fakhr Nabavi, H. Sharifi, A.S. Rouhaghdam, Mater. Chem. Phys. **185**, 162–175 (2017). https://doi.org/10.1016/j.matchemphys.2016.10.019
22. Y. Liao, X. Wang, C. Gao, Q. Zhou, C. Xu, X. Jin, J. Du, W. Xue, Y. Zhang, Trans. Nonferrous Met. Soc. China (English Edition) **34**, 435–452 (2024). https://doi.org/10.1016/S1003-6326(23)66409-X
23. K. Mojsilović, M. Serdechnova, C. Blawert, M.L. Zheludkevich, S. Stojadinović, R. Vasilić, Appl. Surf. Sci. **654**, 159450 (2024). https://doi.org/10.1016/j.apsusc.2024.159450
24. A.G. Settimi, L. Pezzato, A. Longato, K. Brunelli, A. Martucci, S. Gross, M. Dabalà, J. Mater. Eng. Perform. **32**, 5967–5979 (2023). https://doi.org/10.1007/s11665-022-07523-8
25. E. Wierzbicka, B. Pillado, M. Mohedano, R. Arrabal, E. Matykina, Metals (Basel) **10**(7), 916 (2020). https://doi.org/10.3390/met10070916
26. G.H. Oh, J.K. Yoon, J.Y. Huh, J.M. Doh, Corros. Sci. **233**, 112123 (2024). https://doi.org/10.1016/j.corsci.2024.112123
27. G. Yeshmanova, C. Blawert, M. Serdechnova, D.C.F. Wieland, M. Starykevich, E. Gazenbiller, D. Höche, D. Smagulov, M.L. Zheludkevich, Surf. Interfaces **44**, 103797 (2024). https://doi.org/10.1016/j.surfin.2023.103797
28. M. Vakili-Azghandi, A. Fattah-alhosseini, M.K. Keshavarz, Measurement (Lond) **124**, 252–259 (2018). https://doi.org/10.1016/j.measurement.2018.04.038
29. V. Pokhmurskii, H. Nykyforchyn, M. Student, M. Klapkiv, H. Pokhmurska, B. Wielage, T. Grund, A. Wank, J. Therm. Spray Tech. **16**, 998–1004 (2007). https://doi.org/10.1007/s11666-007-9104-x
30. V. Dehnavi, B.L. Luan, D.W. Shoesmith, X.Y. Liu, S. Rohani, Surf. Coat. Technol. **226**, 100–107 (2013). https://doi.org/10.1016/j.surfcoat.2013.03.041
31. S. Akbarzadeh, Y. Paint, M.-G. Olivier, Electrochim. Acta **443**, 141930 (2023). https://doi.org/10.1016/j.electacta.2023.141930
32. L. Pezzato, C. Gennari, M. Franceschi, K. Brunelli, Sci. Rep. **12**, 14329 (2022). https://doi.org/10.1038/s41598-022-18176-x
33. M. Asgari, M. Aliofkhazraei, G. Barati Darband, A. Sabour Rouhaghdam, Surf. Coat. Technol. **383**, 125252 (2020). https://doi.org/10.1016/j.surfcoat.2019.125252
34. M. Toorani, M. Aliofkhazraei, Surf. Interfaces **14**, 262–295 (2019). https://doi.org/10.1016/j.surfin.2019.01.004
35. A. Dasan, P. Ożóg, J. Kraxner, H. Elsayed, E. Colusso, L. Grigolato, G. Savio, D. Galusek, E. Bernardo, Materials **14**(17), 5083 (2021). https://doi.org/10.3390/ma14175083
36. A. Rincón, G. Giacomello, M. Pasetto, E. Bernardo, J. Eur. Ceram. Soc. **37**, 2227–2234 (2017). https://doi.org/10.1016/j.jeurceramsoc.2017.01.012
37. M. O'Hara, S.C. Troughton, R. Francis, T.W. Clyne, Surf. Coat. Technol. **385**, 125354 (2020). https://doi.org/10.1016/j.surfcoat.2020.125354
38. A. Hakimizad, K. Raeissi, M.A. Golozar, X. Lu, C. Blawert, M.L. Zheludkevich, Surf. Coat. Technol. **324**, 208–221 (2017). https://doi.org/10.1016/j.surfcoat.2017.05.068
39. R. Arrabal, M. Mohedano, E. Matykina, A. Pardo, B. Mingo, M.C. Merino, Surf. Coat. Technol. **269**, 64–73 (2015). https://doi.org/10.1016/j.surfcoat.2014.10.048
40. R. Zanini, G. Franceschin, E. Cattaruzza, A. Traviglia, Npj Mater. Degrad. **7**, 38 (2023). https://doi.org/10.1038/s41529-023-00355-4
41. S. Kojima, Solids **1**(1), 16–30 (2021). https://doi.org/10.3390/solids1010003
42. E. Bernardo, G. Scarinci, Ceram. Int. **30**, 785–791 (2004). https://doi.org/10.1016/j.ceramint.2003.09.013
43. J. Schindelin, I. Arganda-Carreras, E. Frise, V. Kaynig, M. Longair, T. Pietzsch, S. Preibisch, C. Rueden, S. Saalfeld, B. Schmid, J.-Y. Tinevez, D. James White, V. Hartenstein, K. Eliceiri, P. Tomancak, A. Cardon, Nat. Methods **9**(7), 676–682 (2012). https://doi.org/10.1038/nmeth.2019

44. A. Pardo, M.C. Merino, A.E. Coy, R. Arrabal, F. Viejo, E. Matykina, Corros. Sci. **50**, 823–834 (2008). https://doi.org/10.1016/j.corsci.2007.11.005
45. R. del Olmo, M. Mohedano, P. Visser, E. Matykina, R. Arrabal, Surf. Coat. Technol. **402**, 126317 (2020). https://doi.org/10.1016/j.surfcoat.2020.126317
46. L. Lorenzetti, L. Tonelli, L. Ceschini, E. Liverani, C. Martini, Wear **510–511**, 204488 (2022). https://doi.org/10.1016/j.wear.2022.204488
47. L. Ceschini, S. Toschi, Friction and wear of aluminum alloys and composites, in *Friction, Lubrication, and Wear Technology*, ed. by G.E. Totten (ASM International, Materials Park, 2017), pp. 509–532
48. ASTM G77-17, Standard Test Method for Ranking Resistance of Materials to Sliding Wear Using Block-on-Ring Wear Test (ASTM International, West Conshohocken, 2022). https://doi.org/10.1520/G0077-17
49. J.A. Williams, R.S. Dwyer-Joyce, Contact between solid surfaces, in *Modern Tribology Handbook*. ed. by B. Bhushian (CRC Press, Boca Raton, 2001), pp.121–162
50. V.S. Egorkin, S.V. Gnedenkov, S.L. Sinebryukhov, I.E. Vyaliy, A.S. Gnedenkov, R.G. Chizhikov, Surf. Coat. Technol. **334**, 29–42 (2018). https://doi.org/10.1016/j.surfcoat.2017.11.025
51. M. Mohedano, M. Serdechnova, M. Starykevich, S. Karpushenkov, A.C. Bouali, M.G.S. Ferreira, M.L. Zheludkevich, Mater. Des. **120**, 36–46 (2017). https://doi.org/10.1016/j.matdes.2017.01.097
52. S. Franz, H. Arab, A. Lucotti, C. Castiglioni, A. Vicenzo, F. Morini, M. Bestetti, Catalysts **10**(3), 325 (2020). https://doi.org/10.3390/catal10030325
53. J.H. Lee, K.H. Jung, S.J. Kim, Appl. Surf. Sci. **516**, 146049 (2020). https://doi.org/10.1016/j.apsusc.2020.146049
54. K.M. Lee, B.U. Lee, S. Il Yoon, E.S. Lee, B. Yoo, D.H. Shin, Electrochim. Acta **67**, 6–11 (2012). https://doi.org/10.1016/j.electacta.2012.01.053
55. A. Fattah-alhosseini, R. Chaharmahali, K. Babaei, J. Magnes. Alloys **8**, 799–818 (2020). https://doi.org/10.1016/j.jma.2020.05.001
56. Q. Huang, L. Liu, Z. Wu, S. Ji, H. Wu, P. Chen, Z. Ma, Z. Wu, R.K.Y. Fu, H. Lin, X. Tian, F. Pan, P.K. Chu, Surf. Coat. Technol. **384**, 125321 (2020). https://doi.org/10.1016/j.surfcoat.2019.125321
57. R.I. Revilla, B. Wouters, F. Andreatta, A. Lanzutti, L. Fedrizzi, I. De Graeve, Corros. Sci. **167**, 108480 (2020). https://doi.org/10.1016/j.corsci.2020.108480
58. G. Bouvet, D.D. Nguyen, S. Mallarino, S. Touzain, Prog. Org. Coat. **77**, 2045–2053 (2014). https://doi.org/10.1016/j.porgcoat.2014.02.008
59. L. Pezzato, V. Angelini, K. Brunelli, C. Martini, M. Dabalà, Trans. Nonferr. Met. Soc. China (English Edition) **28**, 259–272 (2018). https://doi.org/10.1016/S1003-6326(18)64659-X
60. V. Dehnavi, D.W. Shoesmith, B.L. Luan, M. Yari, X.Y. Liu, S. Rohani, Mater. Chem. Phys. **161**, 49–58 (2015). https://doi.org/10.1016/j.matchemphys.2015.04.058
61. M. Zhu, Y. Song, K. Dong, D. Shan, E.H. Han, Electrochim. Acta **411**, 140056 (2022). https://doi.org/10.1016/j.electacta.2022.140056
62. D. Sreekanth, N. Rameshbabu, K. Venkateswarlu, Ceram. Int. **38**, 4607–4615 (2012). https://doi.org/10.1016/j.ceramint.2012.02.040
63. E. Matykina, R. Arrabal, M. Mohedano, B. Mingo, J. Gonzalez, A. Pardo, M.C. Merino, Trans. Nonferr. Met. Soc. China (English Edition) **27**, 1439–1454 (2017). https://doi.org/10.1016/S1003-6326(17)60166-3
64. T. Zehra, M. Kaseem, S. Hossain, Y.G. Ko, Metals (Basel) **11**(8), 1182 (2021). https://doi.org/10.3390/met11081182
65. R. Sola, L. Tonelli, P. Shashkov, T.H. Bogdanoff, C. Martini, Wear **458–459**, 203423 (2020). https://doi.org/10.1016/j.wear.2020.203423